





On-Chip Programmable Nonlinear Optical Signal Processor and Its Applications

Chaoran Huang , Aashu Jha, Thomas Ferreira de Lima , Alexander N. Tait , Bhavin J. Shastri ,
and Paul R. Prucnal, *Life Fellow, IEEE*

(Invited Paper)

Abstract—We introduce an integrated device based on microring resonator (MRR) assisted Mach-Zehnder interferometer (MZI) preceded by a tunable MZ coupler for nonlinear optical signal processing. The novel structure of this device provides both high programmability and switching contrast. These desirable features suggest its potential use as a multi-purpose optical processor providing different high-performance functionalities. We experimentally demonstrate two functionalities using the same device fabricated on a silicon-on-insulator substrate. One functionality is an all-optical thresholder enabling $40\times$ signal contrast improvement, and the other functionality is clock-less pulse carving technique that converts long-pulse signals to short-pulse signals. With these functionalities, we discuss system-level applications of our device in optical interconnects and photonic neural networks.

Index Terms—Neuromorphic photonics, nonlinear silicon photonics, optical signal processing, optical switches, optical pulse shaping.

I. INTRODUCTION

THE development of the silicon-on-insulator (SOI) platforms offers the possibility to integrate optical circuits on a silicon chip [1]. The high refractive index of silicon enables efficient nonlinear light-matter interaction within a short waveguide [2]. The optical nonlinearity can be further enhanced by cavity structures such as microring resonators (MRRs) by increasing instantaneous optical power through coherent power buildup. Silicon nonlinearities are of great interest

owing to their potential applications. Silicon nonlinearities have already been exploited for various all-optical functionalities including all-optical switching [3], logic gates [4], nonreciprocal transmission [5], thresholding [6], signal regeneration [7], etc. The key operation mechanism behind these all-optical functionalities is the power-dependent shift in the resonant spectrum. Therefore, engineering the spectral shape (e.g. on-off contrast and resonance slope) have been extensively studied for the sake of optimizing the performance of all-optical functionalities [8]–[13].

Simple optical circuits configured with a single cavity have a Lorentzian lineshape [14]. As opposed to a single cavity, photonic circuit with multiple coupled cavities can exhibit different lineshapes [8]. Coupled optical cavities warrant research interest because they exhibit a sharp transmission spectrum which can be exploited for applications requiring high switching sensitivities. Various coupled cavity configurations have been investigated both theoretically and experimentally [8]–[11], [15], [16]. Different all-optical functionalities exploiting coupled cavities have also been demonstrated [6], [7], [13].

A desirable feature in a coupled resonant system is the ability to precisely control and reconfigure its spectral shape, i.e. to control the interference (or coupling) conditions between the cavities. Such control enables the same system to have both symmetric and asymmetric spectral shape with different on-off contrast and slope [10], [11], [13], [16]. For example, spectral shapes can be controlled by engineering the nanoscale structures of nanocavities such as photonic crystal cavities rendering small footprint and low power consumption [7], [10]. Alternative approach is to use microheaters which are capable of not only engineering but also programming the spectral shapes after the device is fabricated. Notably, Pérez *et al.* have demonstrated over 20 different functionalities with a seven hexagonal cell structure constituting tunable couplers and microheater based phase actuators [17]. Equipped with the ability of producing various spectral shapes, a programmable coupled resonant system can be engineered as a multi-purpose device for optical signal processing.

This paper is motivated by the interest of employing reconfigurable coupled resonant systems as a *multi-purpose nonlinear optical processor*. We present an MRR-assisted Mach-Zehnder interferometer (MZI) based device that provides flexible programmability in both its spectrum and nonlinear behavior. We

Manuscript received February 23, 2020; revised May 22, 2020; accepted May 23, 2020. Date of publication May 29, 2020; date of current version June 16, 2020. This work was supported in part by the Office of Naval Research (Award N00014-18-1-2297), in part by Defense Advanced Research Projects Agency under Grant HR-00111990049, and in part by National Science Foundation under Grant ECCS-1642962. (Corresponding author: Chaoran Huang.)

Chaoran Huang, Aashu Jha, Thomas Ferreira de Lima, and Paul R. Prucnal are with the Department of Electrical Engineering, Princeton University, Princeton, NJ 08544 USA (e-mail: chaoranh@princeton.edu; aashuj@princeton.edu; tlma@princeton.edu; prucnal@princeton.edu).

Alexander N. Tait is with the Department of Electrical Engineering, Princeton University, Princeton, NJ 08544 USA, and also with the Physical Measurement Laboratory, National Institute of Standards and Technology, Boulder, CO 80305 USA (e-mail: atait@ieee.org).

Bhavin J. Shastri is with the Department of Electrical Engineering, Princeton University, Princeton, NJ 08544 USA, and also with the Department of Physics, Engineering Physics & Astronomy, Queen's University, Kingston, ON K7L 3N6, Canada (e-mail: bhavin.shastri@queensu.ca).

Color versions of one or more of the figures in this article are available online at <https://ieeexplore.ieee.org>.

Digital Object Identifier 10.1109/JSTQE.2020.2998073

experimentally demonstrate the use of such device for all-optical threshold and pulse shaping, and envision its applications in large-scale integrated photonic systems such as photonic neural networks and communication interface of cryogenic system. The contributions, and the organization, of this work are as follows: (1) we propose a practical scheme that allows full control of the interference condition, not shown previously [9], [11], by introducing an MZ coupler (MZC) preceding the MRR-assisted MZI. This design allows to maximize the transmission on-off contrast and slope regardless of the initial coupling condition of the MRR; (2) We demonstrate the programmability of our device in both its linear spectral shape and nonlinear optical bistability in Section II. First, we experimentally characterize the linear transmission spectrum. We achieve an on-off contrast of 47 dB through tuning the biases, even though the initial contrast of the MRR is only 8 dB. Second, we characterize the nonlinear optical bistability in our device using the Coupled-mode theory that considers all the nonlinear effects, as opposed to other theoretical papers where only Kerr effect is considered. Using this theory, we demonstrate the programmability of optical bistability, which paves the way for engineering this device for a variety of optical signal processing applications. (3) We then experimentally demonstrate two high-performance all-optical functionality using the same fabricated device on SOI in Section III and IV. One functionality is an all-optical thresholder (Section III). We demonstrate two optical signals with very close power levels being well distinguished, leading to $40\times$ signal contrast improvement and 5 orders of BER improvement [6]. The other functionality is a clock-less pulse carving technique that converts long-pulse signals to short-pulse signals (Section IV). This functionality has important applications in both digital and analog information processing. We demonstrate the generation of short pulses (100 ps) from long pulses (up to 3 ns) and the improvement of receiver sensitivity; (4) We finally propose two novel system-level applications: cryogenic communication interconnects and neuromorphic photonics, by using the demonstrated optical functionalities in Section V.

II. DEVICE CHARACTERIZATION

A. Device Architecture and Fabrication

Optical nonlinearities in silicon are exploited to engineer devices for all-optical signal processing. The key operation mechanism behind the applications is realized by the power-dependent self-modulation that results in shift in the resonant spectrum. The spectral shape of the resonator determines its switching contrast. We design a programmable device that allows adjustment of spectral shape in order to maximize the extinction ratio and the slope, thus optimizing the switching contrast. Our device consists of an MRR loaded on one arm of an MZI. Near the resonance of the MRR, the signal experiences a drastic linear phase shift, which is further compounded by the power-dependent nonlinear phase shift. The MZI converts the phase shift into intensity change through interference. With a sufficiently large phase difference, the interference between the signals from the two arms of the MZI can switch from constructive to destructive, leading to self-switching. The switching contrast is determined

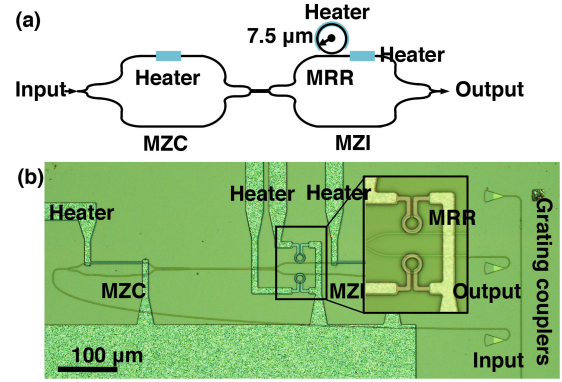


Fig. 1. (a) Schematic illustration of the proposed all-optical thresholder; (b) Optical micrograph of the fabricated device. The resonance of the MRR on the lower arm of MZI is tuned away from the operating wavelength.

by interference conditions. Perfect constructive (or destructive) interference requires the signals traveling in the two MZI arms to have equal amplitudes and an exact 0 (or π) phase difference. To achieve the perfect interference condition, as shown in Fig. 1, we designed a MZ coupler (MZC) preceding the MRR-assisted MZI through a wideband 3 dB coupler. The MZC serves as a three-port optical coupler with tunable power splitting ratio. The bias of the MZC (through the heater) can be adjusted to balance the amplitudes at the two arms of the MZI. On the other hand, the bias of the MZI can be independently tuned to achieve perfect interference condition. The bias on the MRR can also be carefully adjusted to ensure that the device can accommodate different signal wavelengths.

We fabricate our device on a silicon-on-insulator (SOI) substrate. The device consists of fully-etched, 500 nm wide waveguides on a passive-SOI platform with silicon thickness of 220 nm, a 3 m oxide passivation layer, a Ti/W heating filament layer, and an Al routing layer. The MRR has a radius of $7.5\ \mu\text{m}$ and the field coupling coefficient is $\sim 0.6\%$ (gap = 100 nm), yielding a Q-factor of 25000. The resonance of the bottom MRR is not used in the experiment. A microheater on the MRR provides flexible resonance control over a full free spectral range (FSR) (18 nm). Thus, input signals of different wavelengths can be easily accommodated. Two microheaters are deposited on the arms of MZC and MZI. The microheaters are $3\ \mu\text{m}$ wide and $100\ \mu\text{m}$ long, yielding a measured resistance of $\sim 200\ \Omega$. The power consumption for 2π phase tuning is $\sim 33.8\ \text{mW}$. These tunable elements can control the interference condition of the device enabling programmability of the device for different applications. The device insertion loss is $\sim 2\ \text{dB}$ when no biases are applied.

B. Programmable Transmission Spectrum

Here we demonstrate that the resonant spectrum of the device is programmable and can be optimized to achieve large extinction ratio and transmission slope. Typical transmission spectra under different microheater current biases are experimentally measured and shown in Fig. 2. The legends indicate the electronic currents applied to the MZC and MZI respectively resulting in different extinction ratios and resonance shapes. When the

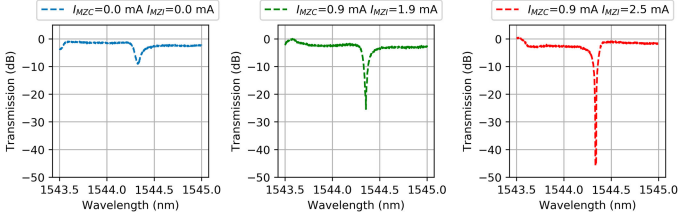


Fig. 2. Measured optical spectrum of the MRR-assisted MZI under different current biases on MZC and MZI.

biases are off (blue curve), the spectrum is asymmetric with an on-off ratio of 8 dB. When the bias currents are on and optimized for maximizing the extinction ratio (red curve), the on-off ratio becomes more than 47 dB. The slope on the short-wavelength side of the resonance increases from 100 dB/nm to 573 dB/nm after the biases are optimized. This highly sensitive transfer spectrum, as a result of perfect interference, is the foundation of high-performance optical signal processing functions introduced in Section III and IV.

C. Programmable Nonlinear Behavior

Silicon photonics offers a suite of nonlinearities including thermo-optic, free-carrier absorption (FCA), free-carrier dispersion (FCD), two-photon absorption (TPA), and the Kerr effect that can be critical for optical devices. All nonlinear optical effects need to be taken into account, in order to correctly model the experimental behavior of optical circuits built on silicon-on-insulator (SOI) platforms. Most theoretical papers have studied the nonlinearity in the MRR-assisted MZI circuits while only focusing on the Kerr effect while ignoring the carrier effects generated from TPA. However, de Lima *et al.* proves that FCD dominates over Kerr in the MRR [18]. To accurately model the nonlinear behaviors in the MRR-assisted MZI circuits, we use the nonlinear coupled-mode theory that encompasses all nonlinear effects. In addition, we compare the nonlinear behavior in the MRR-assisted MZI circuits against that in a single MRR. The results reveal a superior nonlinear behavior of our device via enhanced switching contrast.

Using the coupled-mode theory, nonlinearities in the silicon waveguide including the Kerr effect, TPA, TPA induced FCA and FCD are taken into consideration. Thermo-optic effect is excluded due to its long response time compared to the signal speed of interest. In our simulation model, the MZC and MZI are treated as linear waveguides due to their short lengths. Nonlinear coupled-mode theory is used to study the change in the signal complex amplitude and carrier density in the MRR [19]. The evolution of the normalized complex amplitude a , and the normalized carrier density n is governed by

$$\begin{aligned} \partial a / \partial t = & i(\delta\omega - n_{\text{Kerr}}|a|^2 + \sigma_{\text{fcd}}\alpha_{\text{tpa}}n)a - \\ & - (1 + \alpha_{\text{tpa}}|a|^2 + \gamma_{\text{fca}}\alpha_{\text{tpa}}n)a + \sqrt{\gamma_p P_{\text{in}}(t)} \quad (1a) \end{aligned}$$

$$\partial n / \partial t = |a|^4 - n/\tau, \quad (1b)$$

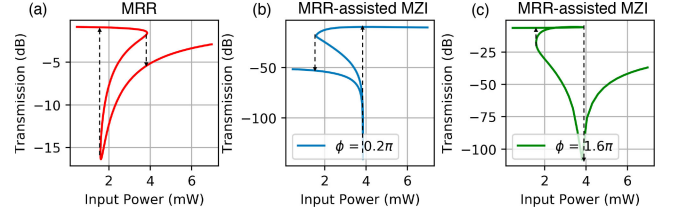


Fig. 3. Stimulated characterization of optical bistability for (a) MRR only, (b) and (c) MRR-assisted MZI with two different phase biases. The black dashed arrow represents the transmission change direction in each hysteresis loop.

where $\delta\omega$ is the frequency detuning between the light source and the MRR resonance; t is the time variable normalized with $\Gamma_0^{-1} = 2Q_L/\omega_0$, Q_L is the total quality factor; P_{in} is the power input, and $(n_{\text{Kerr}}, \alpha_{\text{tpa}}, \sigma_{\text{fcd}}, \gamma_{\text{fca}}, \gamma_p) \propto (n_2\omega_0, \beta_2, \sigma_{e,h}\omega_0, \sigma_{\text{fca}}, \Gamma_c/\Gamma_0^3)$, are the Kerr, TPA, FCD, FCA, and quality factor coefficients, respectively. These equations were simplified from Ref. [19], and renormalized so that the two-photon absorption term only appears in Eq. (1b) [18]. The values of $n_{\text{Kerr}}, \alpha_{\text{tpa}}, \sigma_{\text{fcd}}, \gamma_{\text{fca}}, \gamma_p$ in Eq. (1a) are derived from the parameters given in Ref. [19].

Here we study the programmability of optical bistability in our device by considering all nonlinear optical effects, as opposed to Ref. [11] where only Kerr effect is considered. Optical bistability, manifested as an optical power hysteresis loop, is a powerful phenomena that can be exploited for optical nonlinear signal processing. We compare the optical bistability induced by the MRR-assisted MZI and the MRR, showing that the shape of hysteresis loop can be adjusted using the biases on the MZIs. The signal wavelength used in the simulation is located to the blue side (150 GHz away from the MRR resonance), and the MRR Q factor is 25000, identical to our experimental conditions.

Fig. 3 shows the optical power transmission (defined as the power ratio between the output and input signal) as a function of the incident power for the following cases: MRR only (Fig. 3(a)), and MRR-assisted MZI with two different phase biases (Fig. 3(b), (c)), while keeping the other parameters the same. The hysteresis loop reveals the optical bistability in these optical systems. FCD is the dominating mechanism that contributes to the nonlinear phase [2], [18]. FCD results in a blue shift of the resonance as the incident power is increased. The bistability in a single MRR can be explained as follows. When the incident power is increased, the resonance shifts towards the signal wavelength, causing build-up of the intra-cavity power, which results in positive feedback leading to a sharp transmission edge. At a critical power (i.e. switching power), the transmission direction will reverse and fall abruptly to a lower value. On the other hand, in the case of decreasing incident power, the signal is initially located on the red side of the resonance. Decreasing the optical power leads to resonance shift towards the signal wavelength, which causes the intra-cavity power to build up. This feedback results in an abrupt transition upward. The optical bistability in the MRR thus is a result of the intensity change in the MRR. The ON and OFF switching contrast here relies on the extinction ratio of the MRR, which is subject to fabrication variance and thus difficult to control.

In the case of an MRR-assisted MZI, the optical bistability is a result of the phase change in MRR instead of its intensity change. Here, at the switching power, the signal experiences a phase shift approximately equal to 2π , which causes an abrupt change in transmission. In an MRR-assisted MZI, the switching power is identical to that in MRR. However, the MZI can convert the phase change to intensity change with a large extinction ratio. Therefore, the advantage of using an MRR-assisted MZI is being able to harness the optical phase bistability, which is converted to intensity bistability via the MZI making the switch contrast to over 100 dB as shown in Fig 3(b) and (c). In addition, the shape of hysteresis loop can be adjusted with phase bias ϕ , which is defined as the phase difference between the two MZI arms. One can also program the circulation of the hysteresis loop from clockwise to counterclockwise by controlling the interference conditions: in Fig. 3(b) at phase bias of 0.2π rad, the transition from ON to OFF occurs as the input power decreases, while in Fig. 3(c) at phase bias of 1.6π rad it occurs as the input power increases. This feature can be explained by the different interference conditions: in Fig 3(b), the signal at low power branch first experiences a destructive interference, whereas in Fig 3(c), the signal at low power branch first experiences a constructive interference. In Fig. 3(b) and (c), the power at the two arms of the MZI is set to be balanced at the small input power region.

High switch contrast and programmability are the two notable features of our proposed device. Taking advantage of these features, we demonstrate two fundamental functionalities using the same device in Section III and Section IV. In addition, these fundamental functionalities can serve as the basic building blocks for on-chip photonic systems, as we will discuss in Section V.

III. FUNCTIONALITY I: ALL-OPTICAL THRESHOLDER

Thresholders are at the heart of analog-to-digital converters, comparators and operational amplifiers. Thresholders that are based on simple, effective and integrable all-optical components can have operating speeds well beyond the limit of their electronic counterparts. Therefore, all-optical thresholders have found their unique and indispensable role in a variety of applications which require fast signal processing. Examples include neuromorphic photonics, optical code division multiple access (OCDMA), optical logic gate, optical signal regeneration, and physical layer security, etc [20]–[22]. In this section, we present an all-optical thresholder using the device described in Section II. We also show an example application of the all-optical thresholder in improving the communication link performance. In some communication links, such as in the cryogenic systems described in Section V-A, the signal contrast is severely limited by the small electrical voltages available. We experimentally demonstrate that the all-optical thresholder can make two optical signals with very close power levels be well distinguished, leading to $40\times$ signal contrast improvement and 11 dB receiver sensitivity improvement.

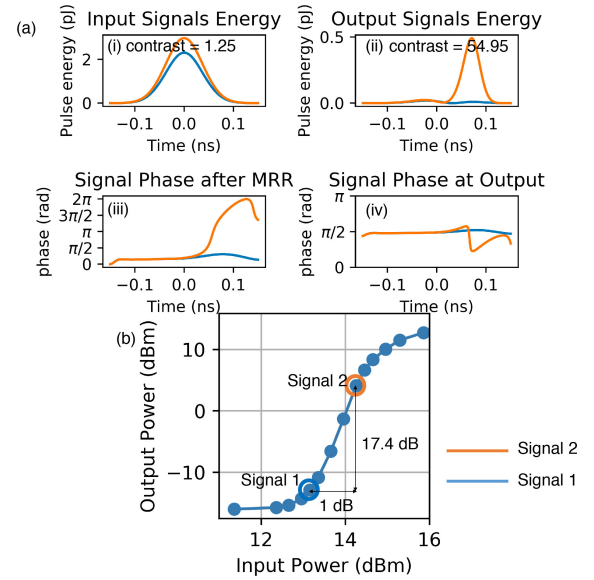


Fig. 4. (a)(i) Input and (ii) output signal waveforms with two different peak powers; signal phase evolution (iii) after the MRR, and (iv) at the threshold output; (b) Power transfer function of the proposed device.

A. Principle and Thresholding Transfer Function

We use the CMT to model the thresholding behavior of the device and explain the principle of our optical thresholder. The input signals are Gaussian pulses with widths of 100 ps. Their wavelength is located at 150 GHz away from the MRR resonance, and the MRR Q factor is 25000. These conditions are consistent with those in the experimental measurement.

Fig. 4(a.i) shows the input signal comprising pulses with two different optical powers. The initial signal contrast (defined as the power ratio of high-power pulse and low-power pulse) is 1.25. Fig. 4(a.iii) shows the nonlinearity-induced intensity dependent phase change in the MRR (derived from Eq. (1a)), which renders an amplitude shift in the MZI output. Along with this phase change, we can optimize the biases applied to the MZC and MZI to maximize the ratio of the peak powers between two output signal levels. This can be accomplished when the phase difference of the higher-power pulse and lower-power pulse is approximately π , and a destructive interference occurs on the lower-power pulse while a constructive interference occurs on the higher-power pulse. As a result, the output pulses (shown in Fig. 4(a. ii)) with significantly improved signal contrast to 54.95 are obtained.

The output pulse width is determined by the time duration that it takes for the signal phase to change from 0 to 2π , which corresponds to the response time of the nonlinearity in the silicon waveguide. As a result, the output pulse duration after the thresholder differs from that of the input. The simulated contrast enhancement and the output pulse width (50 ps) match well with the experimental data. Fig. 4(a.iv) shows the signal phase after the thresholder. Due to the power-dependent nonlinear phase, the output signal experiences a phase distortion. Such a phase distortion can be harmful if the output signal is to be transmitted through an optical fiber with non-negligible dispersion.

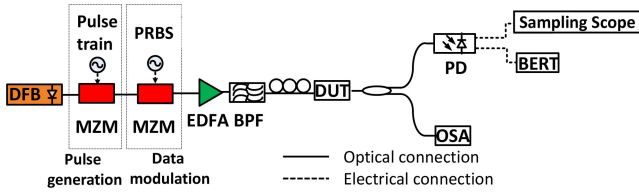


Fig. 5. Experimental Setup: DFB: distributed feedback laser; MZM: Mach-Zehnder; EDFA: erbium-doped fiber amplifier; BPF: bandpass filter; DUT: device under test; OSA: optical spectrum analyzer; OSC: oscilloscope; BERT: bit error rate tester.

However, it is not a concern if the thresholder is operated at the receiver end to process the signals in fiber communication systems. The applications of our thresholder extend beyond fiber communication systems, and can be applied to other applications such as spiking neural networks, chip interconnects where dispersion is negligible.

We characterize the transfer function of the device under a perfect bias condition i.e. optimized power splitting ratio on MZC and phase bias on MZI. The transfer function in Fig. 4(b) reveals a thresholding function with a slope of 17.4.

B. Experimental Demonstration

We conduct an experiment to demonstrate the use of our all-optical thresholder to enhance the signal contrast. A poor signal contrast will lead to degradation of the system quality and result in a large bit error rate (BER) and power penalty of receivers. For a receiver with optical pre-amplifiers (i.e. photodetector noise is signal dependent), power penalty caused by limited signal contrast can be approximately estimated using [23]

$$10 \log \left(\frac{\sqrt{r-1}}{\sqrt{r+1}} \right). \quad (2)$$

where r is the signal contrast. In Eq. (2), shot noise and signal-spontaneous beating noise are considered while thermal noise is ignored [23]. Eq. (2) indicates the receiver sensitivity increases with the signal contrast. Therefore, we show the function of the all-optical thresholder by demonstrating the performance improvement of a communication link.

The experimental setup is shown in Fig. 5. The signal is generated by modulating a distributed feedback (DFB) laser output using two cascaded MZMs. The first MZM is driven by an electrical pulse train generated by a pulse pattern generator (PPG) operating at 10 Gbit/s. The PPG is programmed to output a periodical electrical signal with a “1” followed by 24 “0,” leading to a pulse train with a repetition rate of 400 MHz and a pulsewidth of ~ 80 ps. The second MZM is driven by a 400 Mb/s pseudo randomness binary sequence (PRBS) with a length of 2^7-1 from another PPG. The clocks of the two PPGs are synchronized by connecting the 10 MHz reference clock to each other. This yields a 400 Mb/s return-to-zero (RZ) signal with two different power levels. The contrast between two power levels can be adjusted by tuning the output voltage of the PRBS signal. The data speed is limited by the decay time of the TPA-induced carriers. The optical signal is amplified to

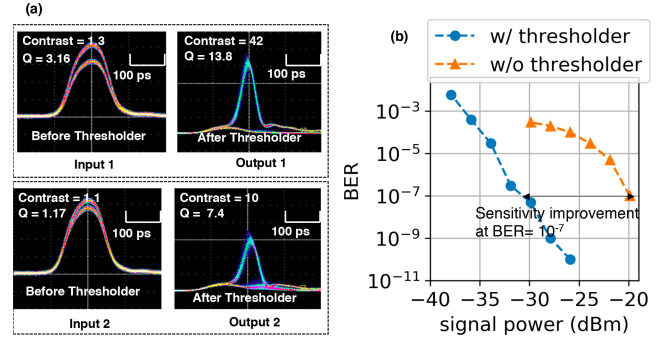


Fig. 6. (a) Eye diagrams of the signals before (left) and after (right) the thresholder for input signal contrast ratios of ~ 1.3 (top) and ~ 1.1 (bottom); (b) Comparison of bit error rate (BER) performance of the system link with and without thresholder. The initial signal contrast ratio is ~ 1.1 .

20dBm by an erbium doped fiber amplifier (EDFA) to trigger nonlinearity in the silicon waveguide and compensate for the fiber-to-chip coupling loss. The optical signal is coupled to the device by free-space coupling through a sub-wavelength grating coupler with ~ 8 dB coupling loss. The eye diagrams of the input and output signals are obtained by photodetectors (Discovery Semiconductor Lab Buddy DSC-R401HG with a bandwidth of 20 GHz) and monitored using a sampling oscilloscope (OSC) (Tektronix DSA8300 with a bandwidth of 70 GHz). The signal optical spectrum is monitored using an optical spectral analyzer (OSA) (APEX AP2440 A). The microheaters are independently driven by computer-controlled current sources to fine tune the bias parameters necessary to attain a high signal contrast ratio.

Fig. 6(a) shows the device performance for two sets of signals with different input signal contrast ratios. Both sets of signals have contrast ratios close to 1, resulting in low signal quality (Q-factor) even though the received average powers (0 dBm) are much higher than the receiver sensitivity. After being processed by the thresholder, the lower power pulses in both signals are fully suppressed. As a result, the signals after thresholding have a significant signal contrast enhancement (~ 40 times for signal 1, and 7.5 times for signal 2), which leads to a Q-factor improvement of 4.4 and 6.3 times for signal 1 and signal 2 respectively. The result confirms that our thresholder works well under signal contrast close to 1.

Fig. 6(b) shows the results of BER measurement of signal 2 using a BER tester (BERT). Assisted with the all-optical thresholder, the communication link can achieve an error-free detection ($\text{BER} = 10^{-9}$) at a received signal power of -27.5 dBm due to the contrast enhancement that results in an opened eye. Without the thresholder, at the same received power (-27.5 dBm), the link has a BER higher than 10^{-4} . The presence of this thresholder can effectively improve the receiver sensitivity by 11 dB at a BER of 10^{-7} (see Fig. 6(b)). According to Eq. (2), the theoretical sensitivity improvement is ~ 12.8 dB which is comparable to the experimental result.

C. Device Speed Discussion

While FCD is the enabling nonlinearity of our thresholder, the time scale of its dynamics is limited by the lifetime of

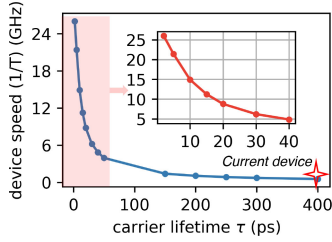


Fig. 7. Device speed as a function of the carrier lifetime; inset: zoomed-in view of the shaded region.

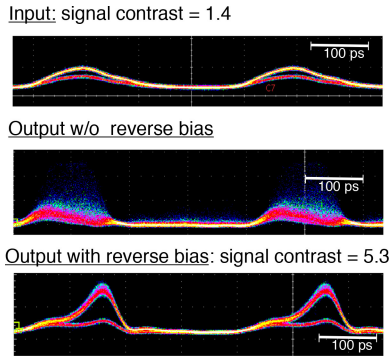


Fig. 8. Eye-diagrams of the input signal and output signals at 2.5 Gbit/s without reverse bias and with reverse bias.

the free carriers, which in turns hinders fast nonlinear signal processing (>10 GHz) in silicon. A well-established technique to effectively reduce the free-carrier lifetime is by active carrier removal, i.e., reverse-biasing a p-n junction transverse to the silicon waveguide to sweep away the free carriers. The carrier lifetime has been shown to be effectively reduced by increasing the reverse-biasing voltage [24]. Here, we first theoretically studied the dependence of device speed on carrier lifetime to assess the speed improvement we can achieve with active carrier removal. We then experimentally demonstrated device speed improvement by incorporating a p-n junction around the MRR.

Using our simulation model described in Eq. (1a) based on CMT, we studied the dependence of device speed on carrier lifetime. In this characterization, the input signal is an impulse with a pulsewidth <1 ps. The device speed is defined as $1/T$, where T is the time that takes to reduce the free carrier number by 99% compared to the peak carrier number. It is worth noting that the definition of T here takes the cavity effect of MRR into consideration, and thus is not equivalent to the carrier lifetime. Fig. 7 shows the device speed as a function of the carrier lifetime. As expected, reducing the carrier lifetime can increase the device speed. However, the improvement in speed comes at the cost of requiring a higher signal power necessary for thresholding. Without carrier removal, our device operated at a speed of 400 Mbit/s (as marked in Fig. 7). The inset of Fig. 7 is a zoomed-in view when the carrier lifetime is smaller than 40 ps. As shown in the inset, our threshold has the potential of working beyond 10 GHz if the carrier lifetime is reduced to ~ 18 ps [24].

We then fabricated and tested the threshold with an embedded PN junction transverse to the MRR, while the remainder of the device architecture stayed the same. Fig. 8 shows the

experimental demonstration of processing speed improvement with our improved device to 2.5 Gbit/s [25]. As evident, without the reverse bias, while there is suppression of the zero-level and some degree of “enhancement” between the two levels, there is substantial noise in the signal that prohibits it from being useful. This noise can be attributed to the free carriers generated via diffusion across the pn junction. However, with the reverse-bias turned on, the noise is eliminated and we achieve a perfect suppression of the zero-level and perfect contrast between the two-levels. We have thus experimentally demonstrated a significant improvement in the device speed via active free-carrier removal, and now have the ability to process signals in the Gbit/s regime. We infer that this speed can be further increased by the use of pulses with shorter widths and higher peak power.

IV. FUNCTIONALITY II: ALL-OPTICAL PULSE CARVING

In this section, we introduce another application of MRR-enhanced MZI: all-optical pulse carving, a clock-less pulse processing technique that converts long-pulse signals to short-pulse signals [26]. Pulse carving has important applications in digital communications and computing. In communication systems, short pulse generation has the benefit of improving the receiver sensitivity [27], reducing the inter-symbol interference and reducing the receiver synchronization complexity. In computing systems, carved pulses have reduced power consumption, and therefore are essential to the systems that require low energy-dissipation for signaling.

Conventional pulse carving technique uses an optical modulator driven by a clock that is synchronized with the incoming signal. On-chip modulators and the matching drive circuits usually require sophisticated circuitry and package design. Our pulse carving technique, on the other hand, exploits the optical nonlinearity in the silicon ring resonator, allowing asynchronous pulse carving driven directly by the optical power of the input signal. This asynchronous feature also offers potential applications to analog signal processing, such as edge detection for image processing.

A. Principle

We use nonlinear CMT to explain the operation principle of pulse carving using our device. The input signal used to illustrate the device operation is a super Gaussian pulse with a pulsewidth of 3 ns. The signal frequency is 150 GHz to the blue side of the MRR resonance. These parameters are consistent with those used in the experiment. We compute the amplitude and phase evolution after the signal propagates through the MRR based on Eq. (1a), and the results are shown in Fig. 9(b). When the input power increases, the output power exhibits strong oscillation because the MRR resonance is shifted driven by the input optical power. As a result of the power oscillation, the signal phase experiences a shift of $\sim 2\pi$.

To show the origins of the power and phase change, the power transmission and phase change are zoomed in near the power oscillation region and are plotted in Fig. 9(c). The interplay between the in-cavity power and free carriers-induced MRR resonance shift lead to the oscillation of the transmission

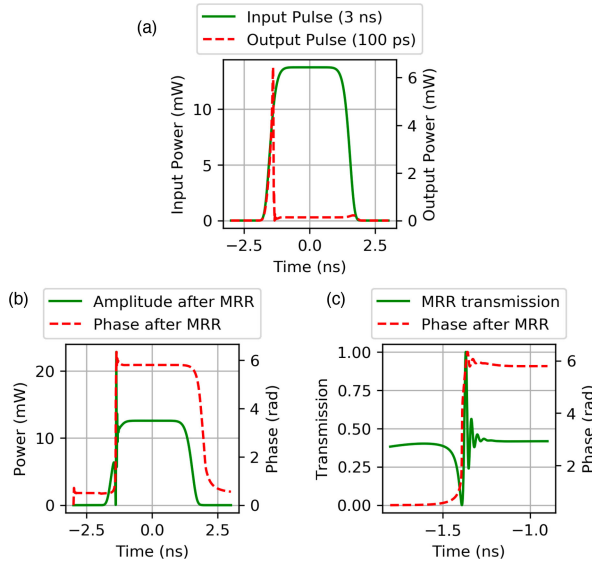


Fig. 9. Simulation of pulse carving. (a) Input signal with a pulsewidth of 3 ns and the corresponding output signal with a pulsewidth of 100 ps; (b) the transmission change and phase change along the pulse duration after the MRR; (c) the zoomed-in view of (b) near the power oscillation region.

spectrum. The reason is explained as follows. As the power of input signal increases, the optical power coupled to the MRR becomes high enough to generate free carriers via two-photon absorption. The free carriers change the refractive index of the ring waveguide and results in the resonance to shift to a shorter wavelength (blue shift). Since the signal is originally at the blue side of the MRR resonance, the resonance shift will bring the signal in resonance which causes the first dip in the transmission spectrum in Fig. 9(c). As the signal power continues increasing, the signal gradually shifts to the red side of the resonance and the transmission increases consequently. When the signal gets out of resonance, the optical power inside the ring cavity decreases which in turn reduces the rate of free carrier generation. As a consequence, the MRR resonance shifts back to a shorter wavelength and the transmission decreases accordingly. The oscillation gradually decays, and finally the system reaches a steady state.

Due to the Kramer-Kronig relation, the sharp transmission changing from 0 to 1 will cause a phase change of $\sim 2\pi$. Now, we optimize the phase biases on the MZC and MZI, such that the signal at ~ -1.42 ns experiences a constructive interference. The signal phase at other times (apart from the short phase transition region) has a π phase difference, and therefore, the signal power will be carved due to the destructive interference. By carefully choosing the biases on MZC and MZI, the pulse width of the signal is carved to 100 ps (Fig. 9(a)).

To understand what determines the pulse width generated using our device, we investigate the relations between 1) input optical power and output pulse width, and 2) input pulse width and output pulse width.

First, we study the output pulse width under different input powers. Three super-Gaussian pulses with peak powers of 21.7 mW, 13.7 mW and 7.2 mW are generated. The three

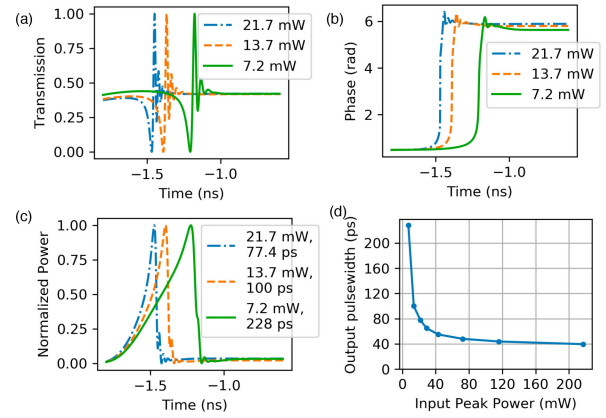


Fig. 10. Characterization of relation between the input signal power and output pulsewidth. (a) The power transmission change, (b) the phase change of signals with three different input powers. Only the zoom-in view near where the transmission oscillation occurs is displayed; (c) the output signals. The input signal pulsewidth are the same for the three signals in (a), (b) and (c); (d) the relation between input power and output pulsewidth.

pulses are identical in shape as shown in Fig. 9(a) and each have a width of 3 ns. The temporal transmission and the phase (only the zoomed-in region) are compared in Fig. 10(a) and (b), respectively. As shown in Fig. 10(a), the higher the optical power, the earlier the onset of transmission oscillation. This is because, for the higher optical power pulses, it takes less time to accumulate enough carriers to bring the signal into the MRR resonance. As a result, the rapid $\sim 2\pi$ phase shift occurs earlier in the pulse with higher input power (Fig. 10(b)). Since the portion of the pulse with a phase value of around 2π will be carved due to destructive interference, the pulse with the highest optical power will generate the shortest output pulse width (Fig. 10(c)). As the input power increases, the output pulse peak gradually shifts towards the edge of the input pulse. At the pulse edge, the required power to further shorten the output pulse width significantly increases, and the output pulse width saturates. The relation between the input power and output pulse width is plotted in Fig. 10(d). The output pulse width decreases as the input power increases, saturating at 40 ps.

Second, we compare the output pulse width under different input pulse widths. Three super-Gaussian pulses are generated, and their pulse widths are 3 ns, 2 ns and 1 ns, respectively. The rising time and the peak power of the three pulses are identical as shown in Fig. 11(a). Fig. 11(c) and (d) show the zoomed-in region of interest where the transmission and phase undergo drastic change (corresponding to the dashed box region in Fig. 11(a)). The time and spectrum of where transmission oscillation and the 2π phase shift occurs are identical in each case, hence resulting in similar output pulse width, as shown in Fig 11(b).

The results in Fig. 10 and 11 indicate that, with sufficient input power, the output pulse width only depends on the pulse shape and the power at the pulse rising edge, while being independent of the input pulse width. This conclusion paves a way for the potential use of this device for edge detection, a fundamental tool in image processing and computer vision.

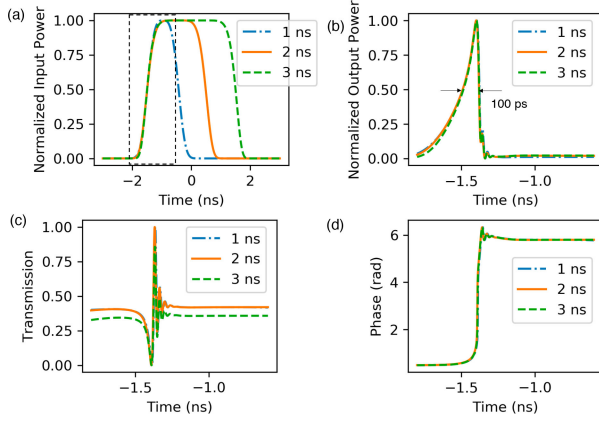


Fig. 11. (a) Input signals with three different pulse widths; (b) output signals; (c) the power transmission change, (b) the phase change of signals with three different input pulse widths. Only the zoom-in view near where the transmission oscillation occurs is displayed.

B. Experimental Demonstration

We use the same experimental setup shown in Fig. 5 for the pulse carving experiment. The input signal is a return-to-zero (RZ) OOK signal generated by modulating a distributed feedback (DFB) laser output using two cascaded MZMs. The first MZM is driven an electrical pulse train generated by a pulse pattern generator (PPG) operating at 10 Gbit/s. The pattern is programmed to output a periodical electrical signal with 100 MHz repetition rate and different duty cycles. The second MZM is driven by a 100 Mb/s PRBS with a length of 2^7-1 from another PPG. This yields a 100 Mb/s RZ-OOK signal with different pulsewidth. The duty cycle of the square wave can be tuned to generate RZ signals with different pulse widths. The optical signal is coupled to the device by free-space coupling through a sub-wavelength grating coupler with 8 dB coupling loss. The optical signal is amplified to 14 dBm by an erbium doped fiber amplifier (EDFA) to trigger the nonlinearity in the silicon waveguide, as well as to compensate for the fiber-to-chip coupling loss. The microheaters are driven by computer-controlled current sources to minimize the output pulse width. We compare the eye diagrams of the input and output signals, and the results are shown in Fig. 12(a). The input signals have pulse widths of 3 ns, 2 ns, 1 ns and 100 ps, respectively. The four signals have approximately identical rising time and average power. Since the average power of four signals are the same, the peak power of each signal decreases as the pulse width increases. Due to the difference in peak power, the output pulse width of signals with 3 ns, 2 ns, 1 ns and 100 ps input pulse width is carved to 100 ps, 88 ps, 78 ps and 63 ps respectively. The output pulse shape and pulse width are consistent with the simulation results.

To evaluate the signal quality of the output signals, we conduct a bit error rate (BER) test. In our experimental system, due to the presence of the optical pre-amplifier (i.e. EDFA), the photodetector noise is signal dependent. In addition, the receiver is sub-optimum because its bandwidth is larger than the signal's bandwidth. Under such conditions, the receiver sensitivity vs.

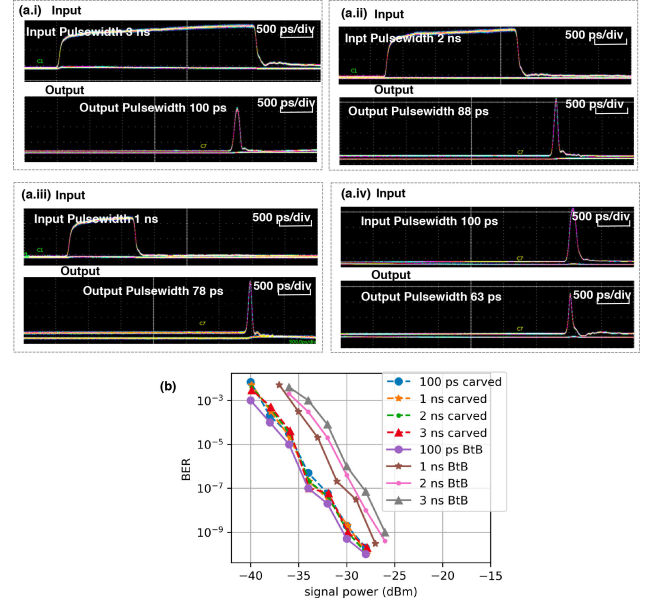


Fig. 12. (a) Eye diagrams and (b) bit error rate (BER) measurement of signals before and after pulse carving.

signal pulsewidth can be estimated by [27]

$$\frac{SE}{2e} \frac{D}{2b_h} \left(1 - \frac{D}{8b_h} \right). \quad (3)$$

where S is the detector's sensitivity, e is the elementary charge, E is the overall optical pulse energy, D is duty cycle, b_h is the receiver bandwidth normalized to the bit rate. Eq. (3) shows the detector sensitivity increases with D when $D/4 < b_h$, which is the case in our experiment. As shown in Fig. 12, an error free operation is achieved for all the output signals. Comparing the back-to-back signals with 1 ns, 2 ns and 3 ns input pulsewidth and their corresponding carved signals, the carved signals provide an receiver sensitivity improvement of 2.5 dB, 3.3 dB and 3.8 dB respectively.

V. INTEGRATED SYSTEMS & APPLICATIONS

A. Application I: Improving the Communication Interface of Cryogenic System

State-of-the-art digital data processing and manipulation can be implemented in superconducting electronics circuitry, based on single-flux quantum (SFQ) logic devices [28]. However, since such systems must be immersed in low temperature (4 K), cryogenic environments, to operate interfacing with ambient temperature ($T = 300$ K) equipment is particularly challenging.

Conventionally, digital input/ output (I/O) interconnect is typically performed through multi-channel coaxial copper wires, which result in significant dispersion and attenuation, as shown in Fig. 13(a). In addition, due to high thermal conductivity of copper, each connection must be thermally connected to multiple intermediate stages to minimize heating.

Digital input/ output (I/O) interconnect can also be typically performed through optical interconnects. A single optical fiber can carry multiple high-bandwidth signals, therefore minimizing

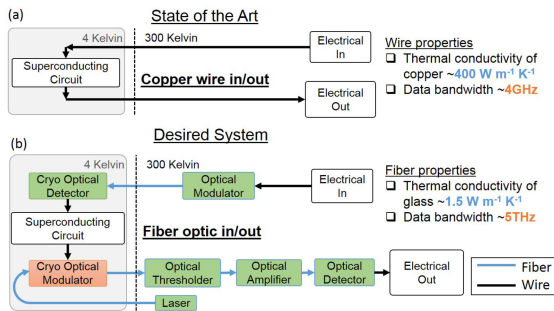


Fig. 13. (a) Interfacing cryogenic setup through copper wire to ambient temperature ($T = 300 \text{ K}$) equipment limit the data bandwidth due to high thermal conductivity of metal contacts. (b) using high bandwidth single optical fiber with low thermal conductivity to communicate with cryogenic system.

the number of physical connections to the cryogenic system, and minimizing the heat leak given an optical fibers low thermal conductivity.

The signal read-out (electrical-to-optical conversion) requires the modulation of flux quantum pulses onto optical carrier waves. Magnetic flux quantum pulses are typically millivolts in amplitude. These ultra-low (aJ) energy pulses make modulation schemes prohibitively challenging. The first key is to design a highly-efficient electrical-optical modulator operated at 4 K and with minimal energy dissipation. However, the small drive voltage from the quantum pulses results in a low signal ER, which hurts the bit-error-rate (BER) of the link.

To relax the requirement on the cryogenic modulator, the all-optical thresholder discussed in Section. III can be added between the modulator and receiver to address the issue of low signal contrast. The proposed system is shown in Fig. 13(b). It is worth mentioning that the functionality of the all-optical thresholder cannot simply be replaced by any optical amplifier or feeding a higher power to the photodetector. The reason is that both the optical amplifier and photodetector has a saturation input power. Beyond the saturation, the signal contrast will further degrade after detection. resulting in a totally closed eye diagram. As opposed to simply increasing the signal power, the optical thresholder removes the residual power on 0-level and enhances the power contrast between 1-level and 0-level. This will allow the amplification of signals without reaching saturation power.

B. Application II: Photonic Neural Network

Programmable Nonlinear Activation Functions: In artificial neural networks, a nonlinear activation function plays an important role in introducing nonlinear mapping between the input and output of a neuron. Implementation of artificial neural networks on photonic platforms have attracted significant research interest due to the inherent advantages of photonics in terms of speed, latency and bandwidth. Various approaches have been proposed to realize nonlinear activation function using photonic hardware [29]–[34].

Our device shows great potential in serving as an all-optical photonic neuron by providing desirable nonlinear activation functions. For example, the high-quality thresholding transfer

function shown in Fig. 4 yields a rectified linear unit (ReLU) shape which is widely used in feedforward neural networks. Moreover, programmability is an essential feature of neurons, because it needs to be trained or reconfigured to synthesize different nonlinear responses in different machine learning tasks. The cascaded MZI structure of our device, together with the heater biases, allows the device to be programmed to realize a variety of nonlinear activation functions.

The main challenge in realizing all-optical nonlinear activation function lies in the weak optical nonlinearity, which results in a relatively high activation threshold. To significantly outperform state-of-the-art electronics, the activation threshold needs to operate at an energy consumption level of fJ/bit, which means the research thrust should be towards simultaneously reducing the device energy and improving the device speed. To this goal, future work requires the development of high-quality microcavity structures rendering high Q factor, small volume V and sharp transfer function, such as photonic crystal Fano resonance [35], to balance the speed and energy tradeoffs. Future work will also explore the consolidation of materials and fabrication platforms that promise high nonlinearity as well as scalability to large photonics integrated circuits [1], [2].

VI. CONCLUSION

This paper introduces an integrated device for nonlinear optical signal processing based on a microring resonator (MRR) assisted Mach-Zehnder interferometer (MZI). We describe the novel design of this device with cascaded MZIs. We demonstrate that such a design allows maximizing the nonlinear switching contrast up to 47 dB regardless of the initial coupling condition of the MRR, as well as providing programmability in both linear transmission and nonlinear bistability.

These desirable features imply the potential use of this device as a multi-purpose optical processor that provide different high-performance functionalities. To verify this claim, we fabricate our devices on a silicon-on-insulator (SOI) substrate, and experimentally demonstrate two all-optical functionalities that harness the optical nonlinearities in silicon waveguide. The first functionality is an all-optical thresholder. Its high-quality step-like transfer function allows two optical signals with very close power levels being well distinguished, leading to $40\times$ signal contrast improvement and 5 orders of BER improvement. The other functionality is all-optical pulse carving, a clock-less pulse processing technique that converts long-pulse signals to short-pulse signals. We demonstrate the generation of short pulses (100 ps) from long pulses (up to 3 ns), together with 3.8 dB receiver sensitivity improvement due to pulse carving.

With these high-performance functionalities, we discuss two system-level applications of our device. One application is to improve the communication interface of cryogenic system. This application relies on the fact that our device can improve the low modulation depth and relax the requirement on the cryogenic modulator. The other application is in photonic neural network. Our device can serve as all-optical nonlinear activation functions. Our device demonstrates high-performance nonlinear transfer functions that can provide complex nonlinear mapping

between neuron input and output. In addition, the transfer functions can be programmed for different computing tasks.

To realize the system-level applications, the future work includes reducing the energy consumption of our device, which requires to reduce the nonlinear switching power and speed at the same time. We will improve the design of microcavity structures rendering high Q factor, small volume V and sharp transfer function to balance the speed and energy tradeoffs. We will also explore the consolidation of materials and fabrication platforms that promise high nonlinearity as well as scalability to large photonics integrated circuits (PICs).

REFERENCES

- [1] D. Thomson *et al.*, "Roadmap on silicon photonics," *J. Opt.*, vol. 18, no. 7, 2016, Art. no. 073003.
- [2] J. Leuthold, C. Koos, and W. Freude, "Nonlinear silicon photonics," *Nature Photon.*, vol. 4, no. 8, pp. 535–544, 2010.
- [3] V. R. Almeida, C. A. Barrios, R. R. Panepucci, and M. Lipson, "All-optical control of light on a silicon chip," *Nature*, vol. 431, no. 7012, pp. 1081–1084, 2004.
- [4] Q. Xu and M. Lipson, "All-optical logic based on silicon micro-ring resonators," *Opt. Express*, vol. 15, no. 3, pp. 924–929, 2007.
- [5] M. Xu, J. Wu, T. Wang, X. Hu, X. Jiang, and Y. Su, "Push-pull optical nonreciprocal transmission in cascaded silicon microring resonators," *IEEE Photon. J.*, vol. 5, no. 1, Feb. 2013, Art. no. 2200307.
- [6] C. Huang *et al.*, "Programmable silicon photonic optical threshold," *IEEE Photon. Technol. Lett.*, vol. 31, no. 22, pp. 1834–1837, Nov. 2019.
- [7] D. A. Bekele *et al.*, "Signal reshaping and noise suppression using photonic crystal Fano structures," *Opt. Express*, vol. 26, no. 15, pp. 19 596–19 605, 2018.
- [8] K. Nozaki, A. Shinya, S. Matsuo, T. Sato, E. Kuramochi, and M. Notomi, "Ultralow-energy and high-contrast all-optical switch involving Fano resonance based on coupled photonic crystal nanocavities," *Opt. Express*, vol. 21, no. 10, pp. 11 877–11 888, 2013.
- [9] L. Zhou and A. W. Poon, "Fano resonance-based electrically reconfigurable add-drop filters in silicon microring resonator-coupled mach-zehnder interferometers," *Opt. Lett.*, vol. 32, no. 7, pp. 781–783, 2007.
- [10] Y. Yu *et al.*, "Fano resonance control in a photonic crystal structure and its application to ultrafast switching," *Appl. Phys. Lett.*, vol. 105, no. 6, 2014, Art. no. 061117.
- [11] Y. Lu, J. Yao, X. Li, and P. Wang, "Tunable asymmetrical Fano resonance and bistability in a microcavity-resonator-coupled mach-zehnder interferometer," *Opt. Lett.*, vol. 30, no. 22, pp. 3069–3071, 2005.
- [12] L. Y. Mario, S. Darmawan, and M. K. Chin, "Asymmetric Fano resonance and bistability for high extinction ratio, large modulation depth, and low power switching," *Opt. Express*, vol. 14, no. 26, pp. 12 770–12 781, 2006.
- [13] L. Stern, M. Grajower, and U. Levy, "Fano resonances and all-optical switching in a resonantly coupled plasmonic-atomic system," *Nature Commun.*, vol. 5, 2014, Art. no. 4865.
- [14] W. Bogaerts *et al.*, "Silicon microring resonators," *Laser Photon. Rev.*, vol. 6, no. 1, pp. 47–73, 2012.
- [15] G. Dong, Y. Wang, and X. Zhang, "High-contrast and low-power all-optical switch using fano resonance based on a silicon nanobeam cavity," *Opt. Lett.*, vol. 43, no. 24, pp. 5977–5980, 2018.
- [16] G. Zhao *et al.*, "Tunable Fano resonances based on microring resonator with feedback coupled waveguide," *Opt. Express*, vol. 24, no. 18, pp. 20 187–20 195, 2016.
- [17] D. Pérez *et al.*, "Multipurpose silicon photonics signal processor core," *Nature Commun.*, vol. 8, no. 1, pp. 1–9, 2017.
- [18] T. F. de Lima *et al.*, "Enhancing soi waveguide nonlinearities via microring resonators," in *Proc. Conf. Lasers Electro-Optics: Sci. Innov.* Optical Society of America, 2019, pp. SW3H–7.
- [19] S. Chen, L. Zhang, Y. Fei, and T. Cao, "Bistability and self-pulsation phenomena in silicon microring resonators based on nonlinear optical effects," *Opt. Exp.*, vol. 20, no. 7, pp. 7454–7468, 2012.
- [20] P. R. Prucnal and B. J. Shastri, *Neuromorphic Photonics*. Boca Raton, FL, USA: CRC Press, 2017.
- [21] K. Kravtsov, P. R. Prucnal, and M. M. Bubnov, "Simple nonlinear interferometer-based all-optical threshold and its applications for optical CDMA," *Opt. Express*, vol. 15, no. 20, pp. 13 114–13 122, 2007.
- [22] C. Huang, P. Y. Ma, B. J. Shastri, P. Mittal, and P. R. Prucnal, "Robustness of optical steganographic communication under coherent detection attack," *IEEE Photon. Technol. Lett.*, vol. 31, no. 4, pp. 327–330, Feb. 2019.
- [23] A. McDonald, R. Fyath, and J. O'Reilly, "Influence of extinction ratio on performance of optical receivers incorporating laser preamplifiers," *Electron. Lett.*, vol. 25, no. 4, pp. 249–250, 1989.
- [24] A. C. Turner-Foster *et al.*, "Ultrashort free-carrier lifetime in low-loss silicon nanowaveguides," *Opt. Express*, vol. 18, no. 4, pp. 3582–3591, 2010.
- [25] A. Jha, C. Huang, T. F. de Lima, and P. R. Prucnal, "High-speed all-optical thresholding via carrier lifetime tunability," *Opt. Lett.*, vol. 45, no. 8, pp. 2287–2290, 2020.
- [26] D. A. Bekele *et al.*, "Pulse carving using nanocavity-enhanced nonlinear effects in photonic crystal Fano structures," *Opt. Lett.*, vol. 43, no. 4, pp. 955–958, 2018.
- [27] P. J. Winzer and A. Kalmár, "Sensitivity enhancement of optical receivers by impulsive coding," *J. Lightw. Technol.*, vol. 17, no. 2, pp. 171–177, 1999.
- [28] Q. P. Herr, A. D. Smith, and M. S. Wire, "High speed data link between digital superconductor chips," *Appl. Phys. Lett.*, vol. 80, no. 17, pp. 3210–3212, 2002.
- [29] A. N. Tait *et al.*, "Silicon photonic modulator neuron," *Phys. Rev. Appl.*, vol. 11, no. 6, 2019, Art. no. 064043.
- [30] I. A. Williamson, T. W. Hughes, M. Minkov, B. Bartlett, S. Pai, and S. Fan, "Reprogrammable electro-optic nonlinear activation functions for optical neural networks," *IEEE J. Selected Topics Quantum Electronics*, vol. 26, no. 1, pp. 1–12, 2019.
- [31] J. Feldmann, N. Youngblood, C. Wright, H. Bhaskaran, and W. Pernice, "All-optical spiking neurosynaptic networks with self-learning capabilities," *Nature*, vol. 569, no. 7755, pp. 208–214, 2019.
- [32] Y. Zuo *et al.*, "All-optical neural network with nonlinear activation functions," *Optica*, vol. 6, no. 9, pp. 1132–1137, Sep. 2019.
- [33] M. Miscuglio *et al.*, "All-optical nonlinear activation function for photonic neural networks," *Opt. Mater. Exp.*, vol. 8, no. 12, pp. 3851–3863, 2018.
- [34] X. Lin *et al.*, "All-optical machine learning using diffractive deep neural networks," *Science*, vol. 361, no. 6406, pp. 1004–1008, 2018.
- [35] K. Nozaki *et al.*, "Sub-femtojoule all-optical switching using a photonic-crystal nanocavity," *Nature Photon.*, vol. 4, no. 7, pp. 477–483, 2010.

Chaoran Huang received the B.Eng. degree in optoelectronic engineering from the Huazhong University of Science and Technology, Wuhan, China, in 2012, and the Ph.D. degrees in electronic engineering (photonics) from The Chinese University of Hong Kong (CUHK), Hong Kong, in 2016.

She is currently a Postdoctoral Research Associate with Princeton University, Princeton, NJ, USA, to develop photonic neural networks and information security system in the photonic layer of communication networks. Her research interests include photonic integrated circuits, optical signal processing, and nonlinear optics with emphasis on applications, such as neuromorphic computing, physical-layer security, and optical communications. Her Ph.D. thesis was selected as finalist for CUHK Engineering Faculty Outstanding Thesis Award, for her work in optical signal processing for advanced fiber communications. She was the recipient of 2019 the Rising Stars Women in Engineering Asia and 2011 China National Scholarship. She has authored or coauthored more than 25 journal articles and 23 conference proceedings. She is serving as an active Reviewer for high quality international journals, and served as a TPC member of international conferences.

Aashu Jha received the B.S. degree in physics and mathematics from Bates College, Lewiston, ME, USA, in 2017, and the M.A. degree in electrical engineering from Princeton University, Princeton NJ, USA, in 2019. She is currently working toward the Ph.D. degree at Princeton University. Her current research interests include nonlinear optics, optical signal processing, neuromorphic photonics, and photonic integrated circuits.

Thomas Ferreira de Lima received the bachelor's and Ingénieur Polytechnicien master's degree from Ecole Polytechnique, Palaiseau, France, with a focus on physics for optics and nanosciences. He is currently working toward the Ph.D. degree in electrical engineering with the Lightwave Communications Group, Department of Electrical Engineering, Princeton University, Princeton, NJ, USA.

His research interests include integrated photonic systems, nonlinear signal processing with photonic devices, spike-timing-based processing, ultrafast cognitive computing, and dynamical light-matter neuro-inspired learning and computing. He has authored or coauthored more than 40 journal or conference papers, contributes to four major open-source projects, and is a contributing author to the textbook *Neuromorphic Photonics*.

Alexander N. Tait received the Ph.D. degree from the Lightwave Communications Research Laboratory, Department of Electrical Engineering, Princeton University, Princeton, NJ, USA, under the direction of P. Prucnal.

He is currently an Electrical Engineer with the Quantum Nanophotonics and Faint Photonics Group, National Institute of Standards and Technology, Boulder, CO, USA, where he was previously an NRC Postdoctoral Fellow. His research interests include silicon photonics, neuromorphic engineering, and superconducting optoelectronics.

Dr. Tait is the recipient of the National Science Foundation (NSF) Graduate Research Fellowship (GRFP) and is a member of the IEEE Photonics Society and the Optical Society of America. He was the recipient of the Award for Excellence from the Princeton School of Engineering and Applied Science, the Best Student Paper Award from the 2016 IEEE Summer Topicals Meeting Series, and the Class of 1883 Writing Prize from the Princeton Department of English. He has authored 11 refereed journal papers and a book chapter, presented at 13 technical conferences, (co)filed eight provisional patents, and contributed to the textbook *Neuromorphic Photonics*.

Bhavin J. Shastri (Senior Member, IEEE) received the Honors B.Eng. (with distinction), M.Eng., and Ph.D. degrees in electrical engineering (photonics) from McGill University, Montreal, QC, Canada, in 2005, 2007, and 2012, respectively. He is currently an Assistant Professor of engineering physics with Queen's University, Kingston, ON, Canada. He was an NSERC and Banting Postdoctoral Fellow from 2012 to 2016 and an Associate Research Scholar from 2016 to 2018 with Princeton University. His research interests are silicon photonics, photonic integrated circuits, neuromorphic computing, and machine learning. He has authored or coauthored more than 50 journal articles and 70 conference proceedings, four book chapters, and given more than 35 invited talks and lectures, including two Keynotes. He is the Co-Author of the book, *Neuromorphic Photonics* (Taylor & Francis, CRC Press, 2017). He was the recipient of the 2014 Banting Postdoctoral Fellowship from the Government of Canada, the 2012 D. W. Ambridge Prize for the top graduating Ph.D. Student, an IEEE Photonics Society 2011 Graduate Student Fellowship, a 2011 NSERC Postdoctoral Fellowship, a 2011 SPIE Scholarship in Optics and Photonics, a 2008 NSERC Alexander Graham Bell Canada Graduate Scholarship, including the Best Student Paper Awards at the 2014 IEEE Photonics Conference, 2010 IEEE Midwest Symposium on Circuits and Systems, the 2004 IEEE Computer Society Lance Stafford Larson Outstanding Student Award, and the 2003 IEEE Canada Life Member Award.

Paul R. Prucnal (Life Fellow, IEEE) received the A.B. degree (graduating *summa cum laude*) in mathematics and physics from Bowdoin College, Brunswick, ME, USA, in 1974, and the M.S., M.Phil., and Ph.D. degrees in electrical engineering from Columbia University, New York, NY, USA, in 1976, 1978, and 1979, respectively, where he did his doctoral work with M. C. Teich. After his doctorate, he joined the faculty with Columbia University in 1979. He is currently a Professor of electrical engineering with Princeton University, Princeton, NJ, USA. He is best known for his seminal work in Neuromorphic Photonics, optical code division multiple access (OCDMA) and the invention of the terahertz optical asymmetric demultiplexor (TOAD). He is currently a fellow of Optical Society of America and National Academy of Inventors. As a member of the Columbia Radiation Laboratory, he performed groundbreaking work in OCDMA and self-routed photonic switching. In 1988, he joined the faculty with Princeton University.

His developmental research on optical CDMA initiated a new research field in which more than 1000 papers have since been published, exploring applications ranging from information security to communication speed and bandwidth. In 1993, he invented the "Terahertz Optical Asymmetric Demultiplexer," the first optical switch capable of processing terabit per second (Tb/s) pulse trains. With support from DARPA in 1990, his group was the first to demonstrate an all-optical 100 gigabit/sec photonic packet switching node and optical multiprocessor interconnect.

He is the author of the book, *Neuromorphic Photonics*, and an Editor of the book, *Optical Code Division Multiple Access: Fundamentals and Applications*. He was an Area Editor for the IEEE TRANSACTIONS ON COMMUNICATIONS. He has authored or coauthored more than 350 journal articles and book chapters and holds 28 U.S. patents. He is a fellow of the Optical Society of America and the National Academy of Inventors, and a member of honor societies, including Phi Beta Kappa and Sigma Xi. He was the recipient of the 1990 Rudolf Kingslake Medal for his paper entitled "Self-routing photonic switching with optically-processed control" and has won multiple teaching awards at Princeton.

He has been instrumental in founding the field of Neuromorphic Photonics and developing the "photonic neuron," a high speed optical computing device modeled on neural networks, as well as integrated optical circuits to improve wireless signal quality by cancelling radio interference.